Geophysical Research Letters

Supporting Information for

Moderate thermal conductivity of Fe-Ni-Si alloy at Earth's core conditions: implications for core thermal evolution and geodynamo

Wen-Pin Hsieh[1,2]*, Yi-Ting Chiang[1,2,3], Frédéric Deschamps[1], Chao-Chih Chen[1], Jen-Wei Chang[1], Daijo Ikuta[4], and Eiji Ohtani[5]

[1]Institute of Earth Sciences, Academia Sinica, Taipei 11529, Taiwan
[2]Department of Geosciences, National Taiwan University, Taipei 10617, Taiwan
[3]Department of Physics, National Taiwan University, Taipei 10617, Taiwan
[4]Institute for Planetary Materials, Okayama University, Misasa, Tottori 682-0193, Japan
[5]Department of Earth Science, Tohoku University, Sendai, Miyagi 980-8578, Japan

Corresponding author: Wen-Pin Hsieh (wphsieh@earth.sinica.edu.tw)

Contents of this file

Introduction

There are one text, seven figures, and two tables that show supporting information to the present study. Figure S1 plots the schematic layout of our experimental setup. Figure S2 shows representative thermal radiation spectra fitted by Planck's black-body radiation function for temperature determination. Figure S3 illustrates an example modelled temperature profile within an LHDAC. Figure S4 and S5 show a set of raw TDTR spectrum for $Fe_{0.85}Ni_{0.06}Si_{0.09}$ at 100.5 GPa/300 K and 95 GPa/2221 K, respectively, fitted by the thermal model. Figure S6 and S7 present analysis of data uncertainty caused by uncertainty of each model parameter. Table S1 and S2 list a set of input parameters used in the thermal model for $Fe_{0.85}Ni_{0.06}Si_{0.09}$ at 100.5 GPa/300 K and 95 GPa/2221 K, respectively.

Text S1. Combination of time-domain thermoreflectance with laser-heated diamond anvil cells

We coupled ultrafast optical pump-probe method—time-domain thermoreflectance (TDTR) with laser-heated diamond anvil cells (LHDACs) to precisely measure the thermal conductivity of Fe and $Fe_{0.85}Ni_{0.06}Si_{0.09}$ under simultaneously high pressure (P)-temperature (T) conditions. Supplementary Fig. S1 schematically shows our experimental setup, where the details of TDTR have been well described in our previous studies, e.g., (Hsieh et al., 2009, 2018, 2020, 2024). To achieve laser heating, we used an infrared laser (wavelength of 1064 nm from IPG YLR fiber laser with a maximum power of 100 W) as the heating source, which passed through a shortpass dichroic mirror (Thorlabs DMSP1000 that reflects the heating laser) and an apochromatic objective lens (US Laser Corp. N3437 with a focal length of 77 mm) that focused the beam on the sample with a typical spot size of ~30 μm.

The thermal radiation emitted from the heated spot of the sample passed through the apochromatic objective lens (US Laser Corp. N3437), the shortpass dichroic mirror (Thorlabs DMSP1000, which also reflected the 1064 nm heating laser reflected from the sample), two dual-notch filters (Semrock NF03-532/1064E-25 that blocked the 1064 nm signal), and finally was collected by an Andor spectrometer (SR-500i-A-R). We determined the temperature of the thermal radiation by fitting the spectrum to Planck's black-body radiation function, focusing on the spectrum range of ~600–700 nm (Meng et al., 2015; Shen et al., 2001; Zhang et al., 2015), see Supplementary Fig. S2 for representative thermal radiation spectra along with their fitted temperature. The system response was calibrated by a standard tungsten lamp (OL550, Optronic Lab) following (Shen et al., 2001; Zhang et al., 2015) and references therein. For each thermal conductivity measurement, we first heated the sample to a target measurement temperature and monitored its stability for ~3–5 minutes, allowing the system to maintain a nearly steady state temperature. We then collected thermal conductivity data (taking ~2 minutes), during which we kept monitoring the temperature, ensuring the measurement temperature remained reasonably stable. Over the ~5–7-minute time window, the temperature fluctuation ΔT_f is typically ~50 K, although in some measurements the ΔT_f could be ~150 K.

Note that due to the currently limited space of experimental setup, the sample was heated at one side of the sample (thermal conductivity was probed from the other side coated with aluminum film). We have calibrated the temperature difference between the two sides of the sample to ~150–250 K by simultaneously measuring the thermal radiation from each side under a laser-heated temperature of ~2000–3000 K. (The thermal radiation from the TDTR-probed side was picked off by a flip reflecting mirror and directed through the other set of optics that is identical to the laser-heated side for temperature measurements.) Such measured temperature difference of ~150–250 K is in good agreement with our modelling by finite difference method (Fig. S3), which solves the steady-state heat diffusion equation in a cylindrical symmetry. For example, we considered a 10 μm-thick Fe disk with a radius of 25 μm sandwiched between 20 μm-thick MgO pressure medium layers (Fig. S3(a)). The sample was heated by a Gaussian-profile laser at its top surface. When compressed to 155 GPa and heated to ~2920 K at its top center region, we found a temperature difference of ~215 K between the top center (heated side) and bottom center (TDTR-probed side), see Fig. S3(b), consistent with our direct measurements (~150–250 K) as well as a literature 3D modelled temperature profile within an LHDAC by (Rainey et al., 2013). Moreover, we also characterized the temperature profile over the sample's top and bottom surfaces, and found that the temperature at the center of the heating spot (~2920 K at r=0 μm) is ~110 K higher than that at radius of 10 μm distant (r=±10 μm, comparable to the radius of our TDTR laser probe spot size, see Fig. S3(c)), which partially contributes to the measurement temperature uncertainty. Finally, we emphasize that the reported temperature for the thermal conductivity measurements shown in this study is the temperature at the TDTR-probed side where we measured the thermal conductivity, rather than the temperature at the laser-heated side.

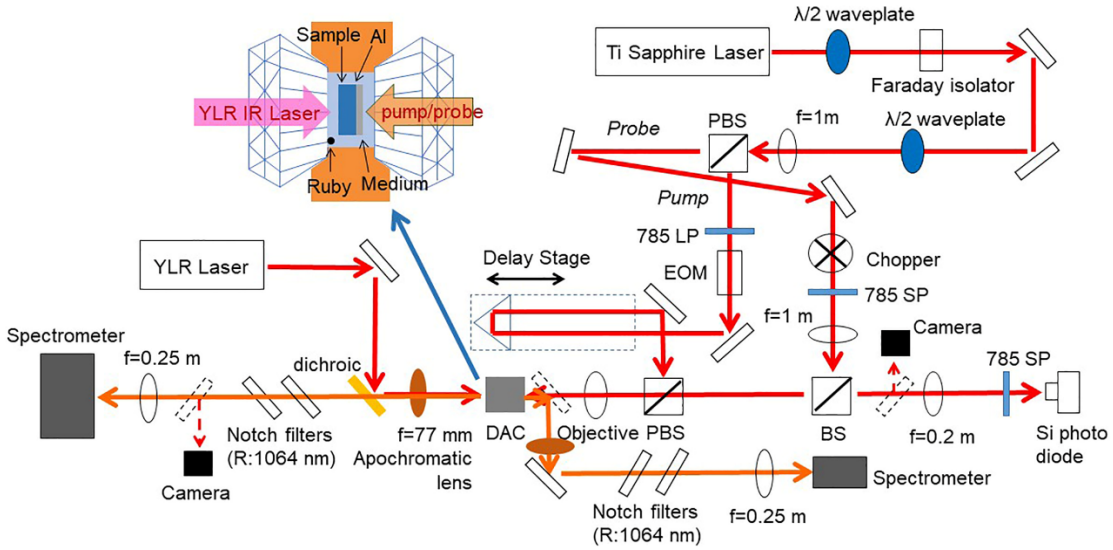

Supplementary Figure S1. Schematic layout of the time-domain thermoreflectance (TDTR at right half) coupled with laser-heated diamond anvil cells (left half). To simultaneously and directly measure the temperature at two sides of the sample, a flip reflecting mirror (the dashed rectangle at the right next to the DAC) was used to direct the thermal radiation from the TDTR-probed side through the other set of optics that is identical to the laser-heated side for temperature measurements.

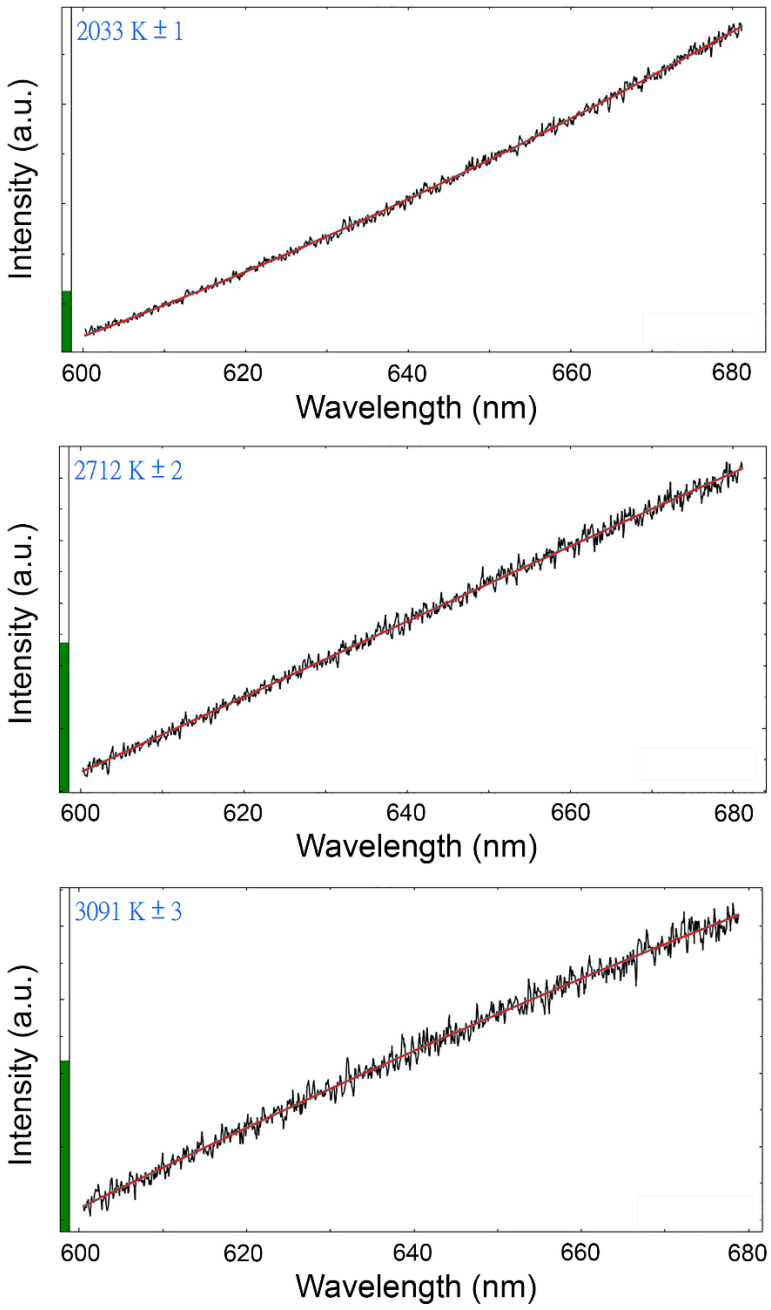

Supplementary Figure S2. Representative thermal radiation spectra fitted by Planck's black-body radiation function (red curve). The fitted temperature of each case is labeled at the upper-left corner. Here the temperature uncertainty represents that caused by the fitting of function.

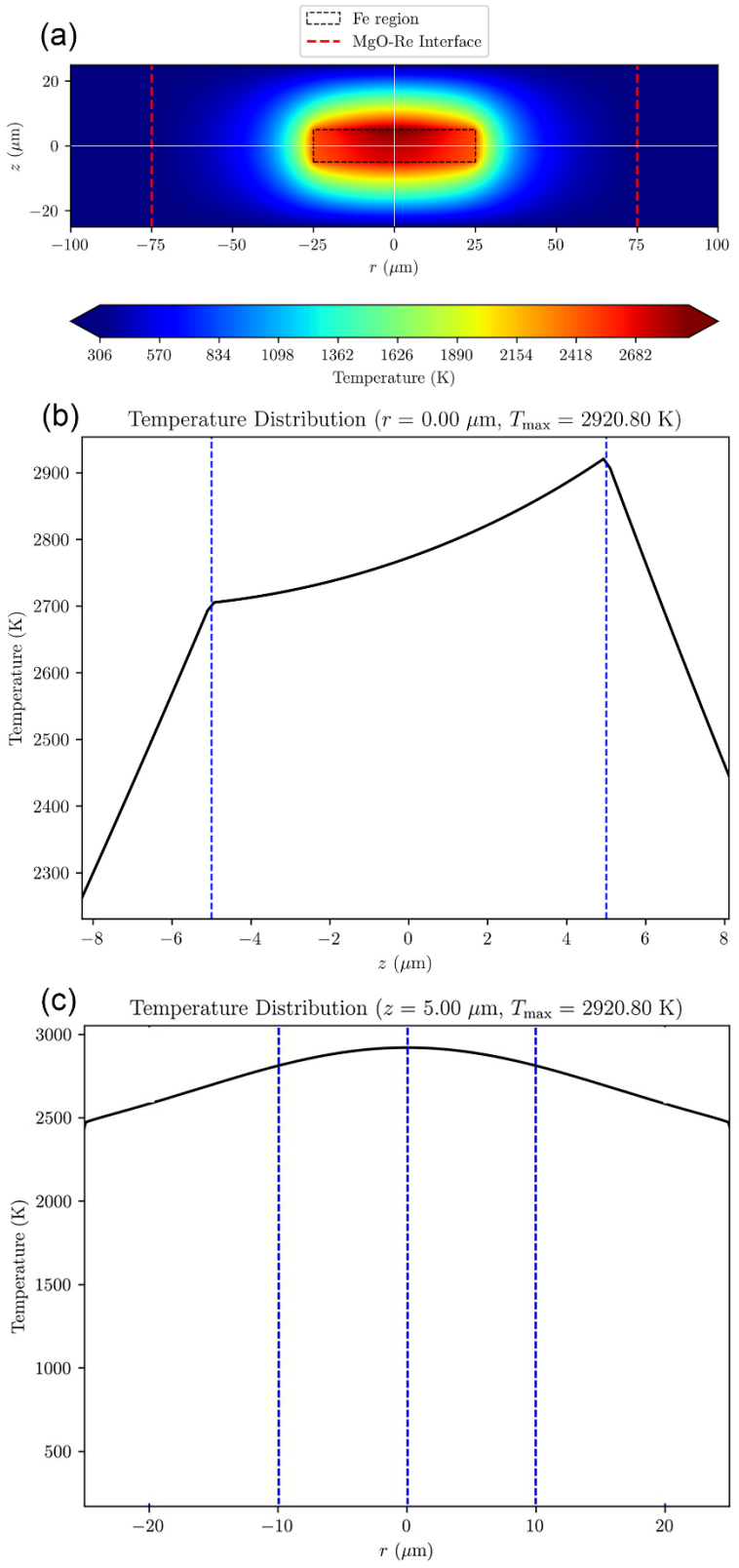

Supplementary Figure S3. (a) Example modelled temperature profile of an Fe sample within an LHDAC using finite difference method solving heat diffusion equation under a

cylindrical coordinate. The sample is sandwiched by MgO nanopowder, compressed to 155 GPa and heated to ~2920 K at its top center region. (b) A modelled temperature difference of ~215 K between the heating side (z= 5 μm) and TDTR-probed side (z= –5 μm) is in good agreement with our directly measured temperature difference from each side of the sample. (c) A modelled temperature profile over the sample's top surface (z= 5 μm). Over the TDTR-probed area (radius of ~10 μm), there is a temperature difference of ~110 K between the center of the heating spot (~2920 K at r=0 μm) and at r=±10 μm distant. A similar temperature difference is observed at the bottom side (z= –5 μm).

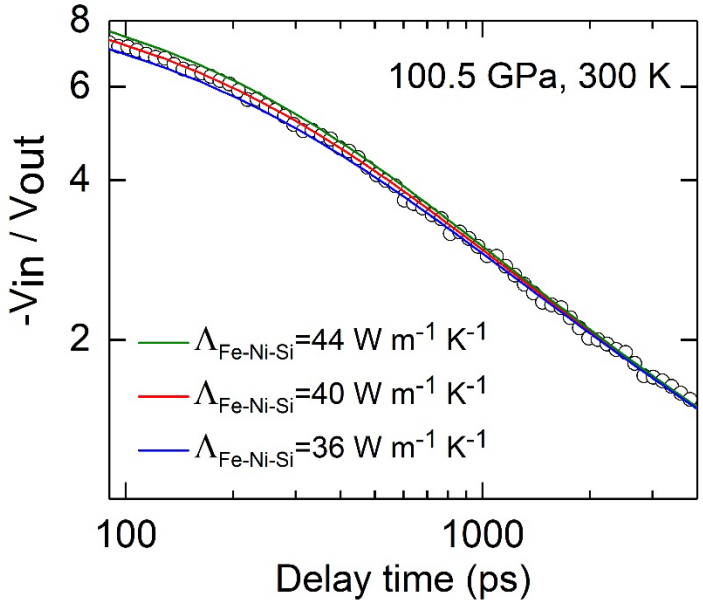

Supplementary Figure S4. Representative TDTR spectrum (open circles) for $Fe_{0.85}Ni_{0.06}Si_{0.09}$ at 100.5 GPa and 300 K along with thermal model calculations (color solid curves). A thermal conductivity $\Lambda_{Fe\text{-}Ni\text{-}Si}$=40 W m^{-1} K^{-1} (red curve) yields the best-fit to the raw TDTR spectrum using a set of input parameters listed in Supplementary Table S1. The data ($-V_{in}/V_{out}$) is most sensitive to the sample's thermal conductivity at few-hundred-picosecond (ps) delay time (Cahill & Watanabe, 2004; Zheng et al., 2007). A 10% difference in $\Lambda_{Fe\text{-}Ni\text{-}Si}$ (green and blue curves) results in a poor fitting to the data, demonstrating the high sensitivity of our data analysis as well as high precision due to our high-quality data.

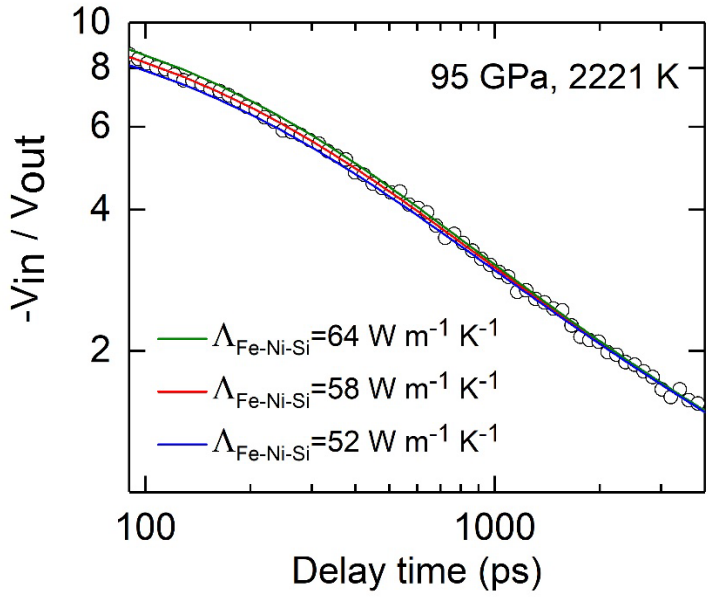

Supplementary Figure S5. Representative TDTR spectrum (open circles) for $Fe_{0.85}Ni_{0.06}Si_{0.09}$ at 95 GPa and 2221 K along with thermal model calculations (color solid curves). Here $\Lambda_{Fe\text{-}Ni\text{-}Si}$=58 W m^{-1} K^{-1} (red curve) yields the best-fit to the raw spectrum using a set of input parameters listed in Supplementary Table S2.

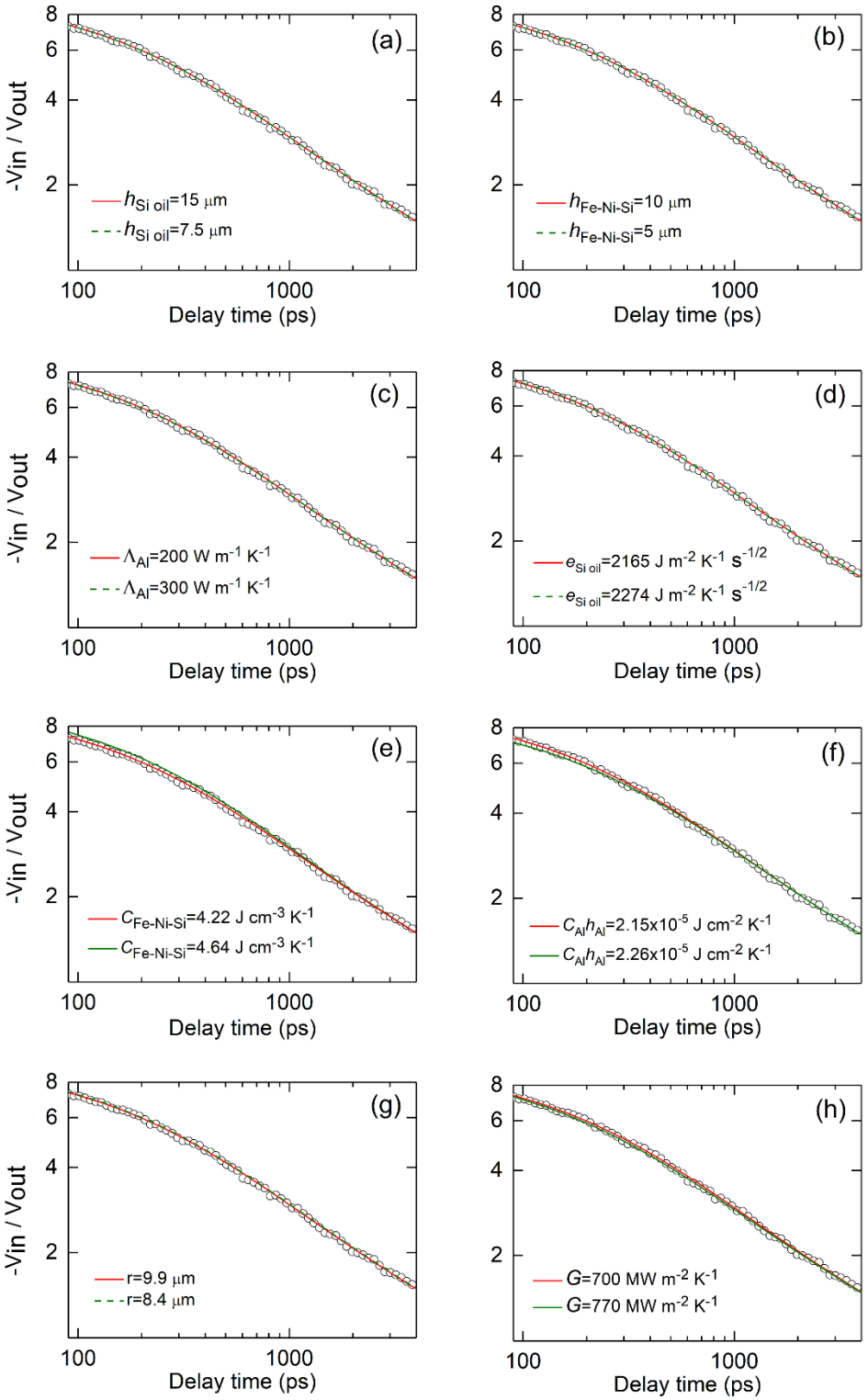

Supplementary Figure S6. Sensitivity tests of the thermal model calculations to key input parameters for $Fe_{0.85}Ni_{0.06}Si_{0.09}$ at 100.5 GPa and room temperature. Here we fix the thermal conductivity of $Fe_{0.85}Ni_{0.06}Si_{0.09}$ ($\Lambda_{Fe\text{-}Ni\text{-}Si}$) at 40 W m^{-1} K^{-1} as obtained in Supplementary Fig. S4. **(a)** and **(b)** Changes in the thicknesses of the pressure medium

137 silicone oil ($h_{\text{Si oil}}$) and $Fe_{0.85}Ni_{0.06}Si_{0.09}$ sample ($h_{\text{Fe-Ni-Si}}$) by as large as 50%, respectively,
138 do not influence the thermal model calculations, suggesting that their individual
139 uncertainty has essentially no effect on the $\Lambda_{\text{Fe-Ni-Si}}$. (**c)** Similarly, an increase in the high
140 thermal conductivity of Al film at high pressures does not affect the thermal model
141 calculation: its uncertainty has no effect on the $\Lambda_{\text{Fe-Ni-Si}}$. (**d)** An example 5% uncertainty in
142 the thermal effusivity of the silicone oil, $e=(\Lambda_{\text{Si}}C_{\text{Si}})^{1/2}$, does not change the thermal model
143 calculation. (**e)** Assuming a 10% uncertainty in the volumetric heat capacity of
144 $Fe_{0.85}Ni_{0.06}Si_{0.09}$, $C_{\text{Fe-Ni-Si}}$, the raw data can be re-fitted well with $\Lambda_{\text{Fe-Ni-Si}}$=37 W m^{-1} K^{-1},
145 suggesting that its uncertainty translates a minor uncertainty of ~7.5%. (**f)** The major
146 uncertainty in our data analysis is the uncertainty in the heat capacity of Al film per unit
147 area (product of Al's volumetric heat capacity and thickness, $C_{\text{Al}}\,h_{\text{Al}}$ (Zheng et al., 2007)).
148 An example 5% uncertainty requires a slightly higher $\Lambda_{\text{Fe-Ni-Si}}$=43 W m^{-1} K^{-1} (~7.5%
149 change) to re-fit the data. (**g)** A 15% uncertainty in the laser spot size and (**h**) a 10% off in
150 the thermal conductance of Al/$Fe_{0.85}Ni_{0.06}Si_{0.09}$ and Al/silicone oil interfaces, G,
151 respectively, have essentially no effect on the thermal model calculations, indicating minor
152 effects on the $\Lambda_{\text{Fe-Ni-Si}}$ due to their uncertainties.
153

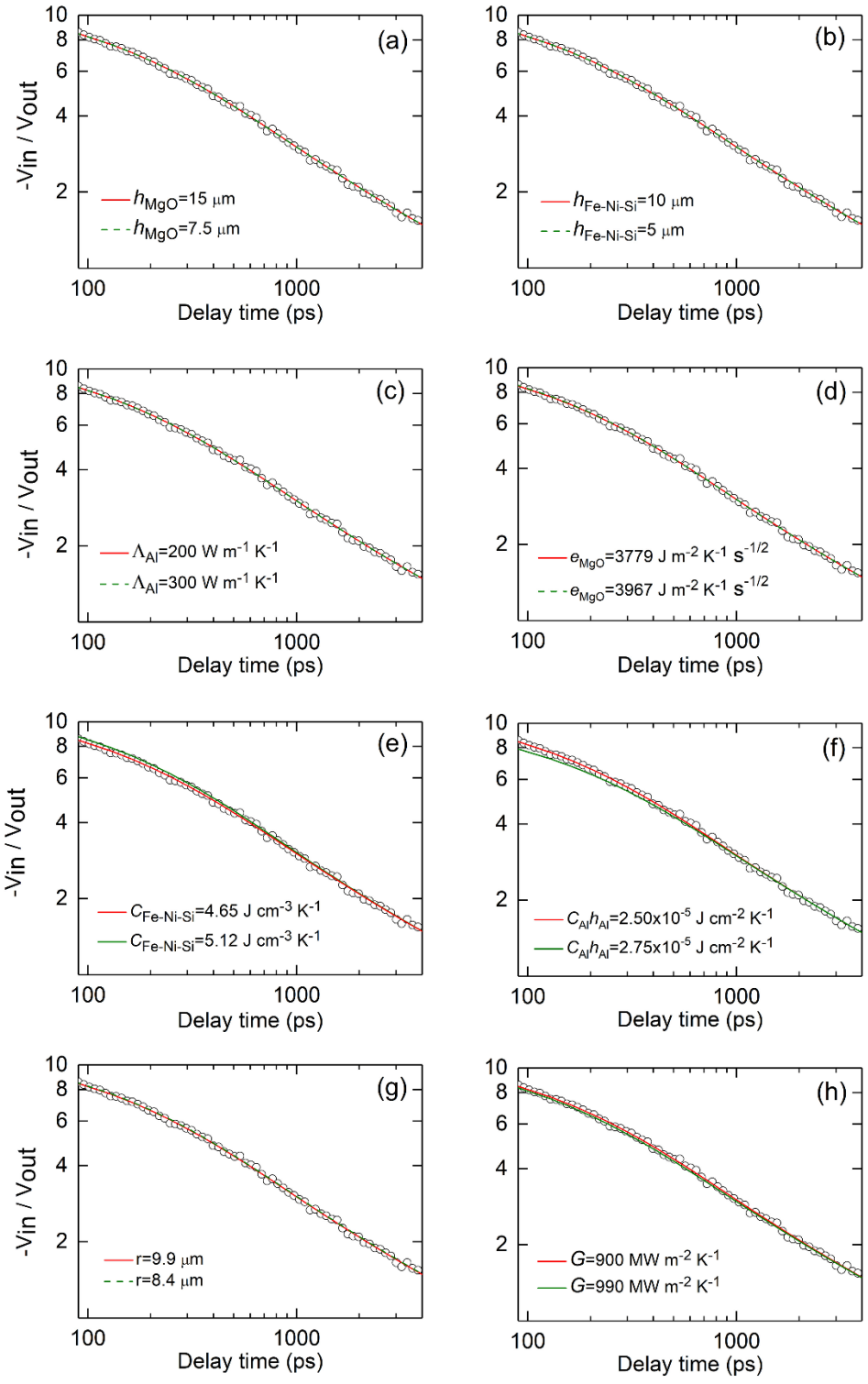

Supplementary Figure S7. Sensitivity tests of the thermal model calculations to key input parameters for $Fe_{0.85}Ni_{0.06}Si_{0.09}$ at 95 GPa and 2221 K. Here we fix the $\Lambda_{Fe\text{-}Ni\text{-}Si}$ at 58 W m^{-1} K^{-1} as obtained in Supplementary Fig. S5. **(a)** and **(b)** Changes in the thicknesses of the pressure medium MgO nanopowder (h_{MgO}) and $Fe_{0.85}Ni_{0.06}Si_{0.09}$ sample ($h_{Fe\text{-}Ni\text{-}Si}$) by as

large as 50%, respectively, has no effect on the thermal model calculations. (**c)** Again, an increase in the high thermal conductivity of Al film at high pressures does not change the thermal model calculation. (**d)** An example 5% uncertainty in the thermal effusivity of the MgO, $e=(\Lambda_{MgO}C_{MgO})^{1/2}$, does not change the thermal model calculation. (**e)** Assuming a 10% uncertainty in the volumetric heat capacity of $Fe_{0.85}Ni_{0.06}Si_{0.09}$, $C_{Fe\text{-}Ni\text{-}Si}$, the raw data can be re-fitted well with $\Lambda_{Fe\text{-}Ni\text{-}Si}$=54 W m^{-1} K^{-1}, suggesting that its uncertainty translates a minor uncertainty of ~7%. (**f)** An example 5% uncertainty in the heat capacity of Al film per unit area requires a slightly higher $\Lambda_{Fe\text{-}Ni\text{-}Si}$=62 W m^{-1} K^{-1} (~7% change) to re-fit the data. (**g)** A 15% uncertainty in the laser spot size and (**h**) a 10% off in the thermal conductance of Al/$Fe_{0.85}Ni_{0.06}Si_{0.09}$ and Al/MgO interfaces, G, respectively, has no effect on the thermal model calculations.

Supplementary Table S1. Input parameters in the thermal model for $Fe_{0.85}Ni_{0.06}Si_{0.09}$ at 100.5 GPa and 300 K in TDTR measurements

P (GPa)	$C_{Fe\text{-}Ni\text{-}Si}$ (J cm^{-3} K^{-1})	C_{Al} (J cm^{-3} K^{-1})	h_{Al} (nm)*	$e=(\Lambda_{Si}C_{Si})^{1/2}$ (J m^{-2} K^{-1} s$^{-1/2}$)	r (μm)	$h_{Fe\text{-}Ni\text{-}Si/Si\ oil}$ (μm)	Λ_{Al} (W m^{-1} K^{-1})	G (MW m^{-2} K^{-1})
100.5	4.22	2.683	80.2	2165	9.9	10/15	200	700

*In this experimental run, the Al thickness at ambient pressure is 94 nm.
$C_{Fe\text{-}Ni\text{-}Si}$: $Fe_{0.85}Ni_{0.06}Si_{0.09}$ heat capacity, C_{Al}: Al heat capacity, h_{Al}: Al thickness, e: silicone oil thermal effusivity, r: laser spot size, $h_{Fe\text{-}Ni\text{-}Si}$: $Fe_{0.85}Ni_{0.06}Si_{0.09}$ thickness, $h_{Si\ oil}$: silicone oil thickness, Λ_{Al}: Al thermal conductivity, G: thermal conductance of Al/$Fe_{0.85}Ni_{0.06}Si_{0.09}$ and Al/silicone oil interfaces.

Supplementary Table S2. Input parameters in the thermal model for $Fe_{0.85}Ni_{0.06}Si_{0.09}$ at 95 GPa and 2221 K in TDTR measurements

P (GPa)	$C_{Fe\text{-}Ni\text{-}Si}$ (J cm^{-3} K^{-1})	C_{Al} (J cm^{-3} K^{-1})	h_{Al} (nm)*	$e=(\Lambda_{MgO}C_{MgO})^{1/2}$ (J m^{-2} K^{-1} s$^{-1/2}$)	r (μm)	$h_{Fe\text{-}Ni\text{-}Si/MgO}$ (μm)	Λ_{Al} (W m^{-1} K^{-1})	G (MW m^{-2} K^{-1})
95	4.65	3	83.2	3779	9.9	10/15	200	900

*In this experimental run, the Al thickness at ambient pressure is 97.3 nm.
$C_{Fe\text{-}Ni\text{-}Si}$: $Fe_{0.85}Ni_{0.06}Si_{0.09}$ heat capacity, C_{Al}: Al heat capacity, h_{Al}: Al thickness, e: MgO nanopowder thermal effusivity, r: laser spot size, $h_{Fe\text{-}Ni\text{-}Si}$: $Fe_{0.85}Ni_{0.06}Si_{0.09}$ thickness, h_{MgO}: MgO thickness, Λ_{Al}: Al thermal conductivity, G: thermal conductance of Al/$Fe_{0.85}Ni_{0.06}Si_{0.09}$ and Al/MgO interfaces.

The input parameters for all the data in Figs. 1 and 2 in main text are available at (Hsieh, Chiang, et al., 2025) https://zenodo.org/records/17184617.

Supplementary References

Cahill, D. G., & Watanabe, F. (2004). Thermal conductivity of isotopically pure and Ge-doped Si epitaxial layers from 300 to 550 K. *Phys. Rev. B*, *70*(23), 235322. https://doi.org/10.1103/PhysRevB.70.235322

Hsieh, W.-P., Chen, B., Li, J., Keblinski, P., & Cahill, D. G. (2009). Pressure tuning of the thermal conductivity of the layered muscovite crystal. *Physical Review B - Condensed Matter and Materials Physics*, *80*(18), 180302. https://doi.org/10.1103/PhysRevB.80.180302

Hsieh, W.-P., Deschamps, F., Okuchi, T., & Lin, J. F. (2018). Effects of iron on the lattice thermal conductivity of Earth's deep mantle and implications for mantle dynamics. *Proceedings of the National Academy of Sciences of the United States of America*, *115*(16), 4099–4104. https://doi.org/10.1073/pnas.1718557115

Hsieh, W.-P., Goncharov, A. F., Labrosse, S., Holtgrewe, N., Lobanov, S. S., Chuvashova, I., et al. (2020). Low thermal conductivity of iron-silicon alloys at Earth's core conditions with implications for the geodynamo. *Nature Communications*, *11*(1), 3332. https://doi.org/10.1038/s41467-020-17106-7

Hsieh, W.-P., Deschamps, F., Tsao, Y.-C., Yoshino, T., & Lin, J.-F. (2024). A thermally conductive Martian core and implications for its dynamo cessation. *Sci. Adv.*, *10*, eadk1087.

Meng, Y., Hrubiak, R., Rod, E., Boehler, R., & Shen, G. (2015). New developments in laser-heated diamond anvil cell with in situ synchrotron x-ray diffraction at High Pressure Collaborative Access Team. *Review of Scientific Instruments*, *86*(7), 072201. https://doi.org/10.1063/1.4926895

Rainey, E. S. G., Hernlund, J. W., & Kavner, A. (2013). Temperature distributions in the laser-heated diamond anvil cell from 3-D numerical modeling. *Journal of Applied Physics*, *114*(20), 204905. https://doi.org/10.1063/1.4830274

Shen, G., Rivers, M. L., Wang, Y., & Sutton, S. R. (2001). Laser heated diamond cell system at the advanced photon source for in situ x-ray measurements at high pressure and temperature. *Review of Scientific Instruments*, *72*(2), 1273–1282. https://doi.org/10.1063/1.1343867

Zhang, J. S., Bass, J. D., & Zhu, G. (2015). Single-crystal Brillouin spectroscopy with CO2 laser heating and variable q. *Review of Scientific Instruments*, *86*(6), 063905. https://doi.org/10.1063/1.4922634

Zheng, X., Cahill, D. G., Krasnochtchekov, P., Averback, R. S., & Zhao, J. C. (2007). High-throughput thermal conductivity measurements of nickel solid solutions and the applicability of the Wiedemann-Franz law. *Acta Materialia*, *55*(15), 5177–5185. https://doi.org/10.1016/j.actamat.2007.05.037